IEEE Photonics Journal
An IEEE Photonics Society Publication

Open Access

A Compact Ultrabroadband Polarization Beam Splitter Utilizing a Hybrid Plasmonic Y-Branch

Volume 8, Number 4, August 2016

Ting Hu
Haodong Qiu
Zecen Zhang
Xin Guo
Chongyang Liu
Mohamed S. Rouifed
Callum G. Littlejohns
Graham T. Reed
Hong Wang

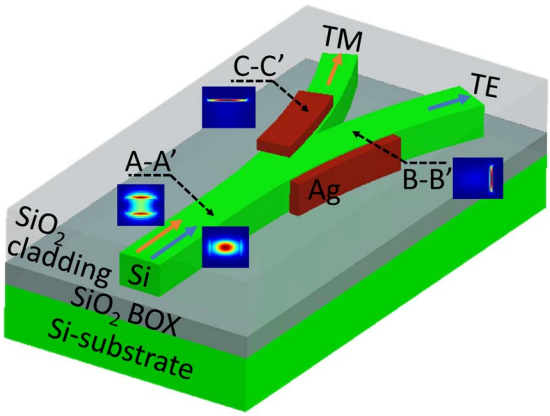

DOI: 10.1109/JPHOT.2016.2585113
1943-0655

IEEE photonics SOCIETY

IEEE

A Compact Ultrabroadband Polarization Beam Splitter Utilizing a Hybrid Plasmonic Y-Branch

Ting Hu,[1] Haodong Qiu,[1] Zecen Zhang,[1] Xin Guo,[1] Chongyang Liu,[2] Mohamed S. Rouifed,[1] Callum G. Littlejohns,[1] Graham T. Reed,[3] and Hong Wang[1]

[1]School of Electrical and Electronic Engineering, Nanyang Technological University, Singapore 639798
[2]Temasek Laboratories, Nanyang Technological University, Singapore 639798
[3]Optoelectronics Research Centre, Building 53, University of Southampton, Southampton SO17 1BJ, U.K.

DOI: 10.1109/JPHOT.2016.2585113

Manuscript received May 25, 2016; revised June 21, 2016; accepted June 22, 2016. Date of publication June 28, 2016; date of current version July 11, 2016. This work was supported in part by the National Research Foundation Singapore under Grant NRF-CRP12-2013-04 and in part by the Nanyang Technological University-A*Star Silicon Technologies Centre of Excellence. The work of G. T. Reed was supported by a Royal Society Wolfson Research Merit Award through the Wolfson Foundation and the Royal Society. Corresponding author: H. Wang (e-mail: ewanghong@ntu.edu.sg).

Abstract: A compact and ultrabroadband polarization beam splitter (PBS) utilizing a hybrid plasmonic Y-branch (HPYB) on a silicon-on-insulator (SOI) platform is proposed and numerically demonstrated. The HPYB consists of a vertical hybrid plasmonic waveguide (HPW) and a horizontal HPW formed by silicon (Si) and silver (Ag) strip waveguides sandwiched with a silicon dioxide (SiO_2) layer, in which the vertical and horizontal hybrid plasmonic modes (HPMs) are excited by the input transverse electric (TE) and transverse magnetic (TM) modes, respectively. The HPMs are split into different ports and coupled back to TE and TM modes to implement the polarization splitting function. A simplified and compact HPYB is robust for the HPMs' generation. The structure is wavelength insensitive since the HPMs' excitation is weakly correlated to the optical wavelengths. The simulation results show that the HPYB-based PBS has a compact footprint of $5 \times 1.8\ \mu m^2$ and an ultralarge working bandwidth of 285 nm, with the polarization crosstalk < −10 dB and the worst-case TE (TM) mode insertion loss of −1.53 (−2.35) dB. The device also exhibits a large fabrication tolerance of 210-nm variation (from −100 to 110 nm) to the waveguide width for both polarizations.

Index Terms: Integrated optics devices, polarization-selective devices, plasmonics.

1. Introduction

Silicon-on-insulator (SOI) is an attractive platform to implement high-density, cost-effective, and energy-saving integration photonic circuits. The feature of high refractive index contrast between silicon (Si) and silicon dioxide (SiO_2) brings the advantage of making Si photonic device compact. However, this leads to strong birefringence and results in polarization sensitive problems in sub-micron Si photonic components so that the control and management of polarizations in silicon photonics is becoming important [1]. The polarization beam splitter (PBS), which has the function of splitting transverse-electric (TE) and transverse-magnetic (TM) polarization beams to

different optical paths, is a key component for polarization manipulation. A lot of work on PBSs built by all-dielectric waveguides has been reported. The Mach–Zehnder interferometer (MZI) based PBS demonstrated in [2] has a length of 200 μm, which is unfavorable for the high density integration of photonic circuits due to the large footprint. The Bragg grating-assisted couplers based PBSs [3]–[5], with the device length of tens micrometers, usually have a working bandwidth below 50 nm due to the limited optical filter bandwidth. The directional couplers [6], [7] and multimode interferometers (MMIs) [8], [9] based PBSs have the compact footprint with length and width around or less than 10 μm. For these two types of PBSs, the former ones have larger bandwidth with the same extinction ratio (ER). However, the bandwidth with 10 dB ER of the PBS proposed in [6] is below 200 nm. Recently, Shen *et al.* experimentally demonstrated a PBS based on free-form metamaterials [10]. The device has an ultra-compact footprint of 2.4×2.4 μm^2, but the bandwidth with 10 dB ER is only 32 nm. Because of the large birefringence of metals, surface plasmon polarizations (SPPs) can be excited by light with specific polarizations, which provide alternative solutions for the PBS design. Kim *et al.* transformed the 2-D SPPs based PBS [11] to a three dimensional structure and improved the device performance [12]. The device can work within a bandwidth of 280 nm, with the insertion loss $(\mathrm{IL}) < -3$ dB and $\mathrm{ER} > 15$ dB. However, the device has a vertical taper in the output waveguide, which is a challenge to the fabrication process. A hybrid plasmonic waveguide (HPW) with a dielectric cylinder above a metal surface has been reported to take place of SPPs for realizing long propagation distance with lower propagation loss [13], but the cylinder structure is difficult to fabricate by the planar lightwave circuit technology. Based on this concept, Dai *et al.* proposed the rectangular metal-SiO_2-Si HPW on SOI platform, which reduces the propagation loss and increases the propagation distance to be on the order of 100 μm [14]. In their following work, the silver (Ag)-SiO_2-Si based directional coupler (DC) was proposed to realize the PBS [15].

In this paper, we propose a PBS by using a hybrid plasmonic Y-branch (HPYB) on the SOI platform. For the PBSs reported in [11] and [12], the SPPs serve as the assisted medium to couple TE (TM) mode to the cross output, while in our proposed PBS, the vertical and horizontal hybrid modes are excited by the input TE and TM modes directly and then split to different ports, which contributes to the simplified structure and ultra-large working bandwidth of the device. Another advantage is that it is unnecessary to satisfy the phase-matching condition which is required in the HPW DC based PBS [15], [16]. A compact footprint of 5×1.8 μm^2 and an ultrabroad bandwidth of 285 nm from 1.861 to 2.146 μm within a crosstalk $(\mathrm{CT}) < -10$ dB (an equivalent $\mathrm{ER} > 10$ dB) and an $\mathrm{IL} < -2.35$ dB are demonstrated for the proposed PBS by numerical simulations. It has a larger bandwidth than those reported in [2]–[6], [10]–[12], and [16], and its footprint is comparable to the most compact PBSs [6]–[12], [15], [16], with the trade-off of a slightly higher IL. The SPPs based PBS in [12] has a proximate bandwidth to our proposed device with a better ER, but its IL is higher and the fabrication of its vertical taper is a challenging job. Further analysis reveals that the proposed PBS has large fabrication tolerance, which allows waveguide width variation up to 210 nm. Moreover, the working spectral range covers the mid-infrared wavelength of 2 μm, leading to potential applications in the sensing systems for gas detection, such as carbon dioxide (CO_2) and ammonia (NH_3), which have large absorption around this wavelength [17], [18].

2. Principle and Device Designs

The schematic of the proposed PBS is shown in Fig. 1(a). The input section is a straight Si waveguide with the width of W and height of H. Its cross section is shown in Fig. 1(c). The two bending Si waveguides have the same height with the input waveguide and the radii of $R_1 = R_2 = 20$ μm [see Fig. 1(b)]. A vertical HPW is constructed on the right hand bending Si waveguide sidewall in the form of an Ag strip and a slot SiO_2 layer between them. As shown in Fig. 1(d), the width of Si, Ag and SiO_2 of the vertical HPW are denoted as W_v, W_{Ag}, and W_s, respectively. The left bending Si waveguide has an Ag strip above it with an intermediate SiO_2 layer which together form the horizontal HPW, the cross section of which is shown in Fig. 1(e). The height of SiO_2, Ag, and

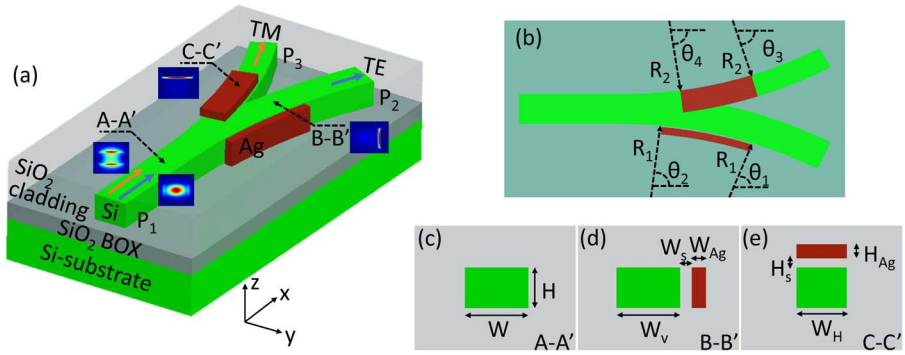

Fig. 1. Schematic of the proposed PBS. (a) Three-dimensional view, (b) the top view, and the cross section of (c) A-A', (d) B-B', and (e) C-C'.

the width of Si of the horizontal HPW are H_s, H_{Ag} and W_H, respectively. The working principle of the proposed PBS is as follows: The input light with TE polarization launched into Port 1 (P_1) excites the hybrid plasmonic mode (HPM) in the vertical HPW and then is guided to the output port 2 (P_2), while the TM polarization light sent into P_1 excites the HPM in the horizontal HPW and transmits to the output port 3 (P_3). The electrical fields of TE mode, TM mode, vertical HPM and horizontal HPM are plotted as insets in Fig. 1(a). To characterize the device performance, the IL and CT of different modes are defined as the following (expressed in decibels):

$$\mathrm{IL_{TE}} = 10 \cdot \log_{10}\left(\frac{P_2^{\mathrm{TE}}}{P_1^{\mathrm{TE}}}\right) \tag{1}$$

$$\mathrm{IL_{TM}} = 10 \cdot \log_{10}\left(\frac{P_3^{\mathrm{TM}}}{P_1^{\mathrm{TM}}}\right) \tag{2}$$

$$\mathrm{CT_{TE}} = 10 \cdot \log_{10}\left(\frac{P_3^{\mathrm{TE}}}{P_3^{\mathrm{TM}}}\right) \tag{3}$$

$$\mathrm{CT_{TM}} = 10 \cdot \log_{10}\left(\frac{P_2^{\mathrm{TM}}}{P_2^{\mathrm{TE}}}\right) \tag{4}$$

where P_i^{TE} $(i = 1, 2, 3)$ represents the optical power at port i with TE mode launched, and P_i^{TM} $(i = 1, 2, 3)$ is the optical power at port i with TM mode injected. $\mathrm{IL_{TE}}$ and $\mathrm{CT_{TE}}$ are the IL and CT of TE mode. $\mathrm{IL_{TM}}$ and $\mathrm{CT_{TM}}$ represent the IL and CT of TM mode. One can see from (3) and (4) that the absolute values of $\mathrm{CT_{TE}}$ and $\mathrm{CT_{TM}}$ are equal to the ER of P_3 and P_2, respectively.

The 3-D finite difference time domain (3-D FDTD) method is employed to simulate the proposed PBS. The investigations convey that the starting and ending angles of the bending Ag strip are important to realize the polarization splitting function. The starting and ending angles of the bottom (up) Ag strip are defined as θ_1 and θ_2 (θ_3 and θ_4), respectively, as shown in Fig. 1(b). Preliminary simulations predict that the device can realize the polarization splitting well when the beginning (θ_1, θ_3) and ending angles (θ_2, θ_4) are around 79° and 85°. The simulation of fine tuning θ_1 and θ_2 with setting $\theta_3 = 79^\circ$ and $\theta_4 = 84^\circ$ is then carried out. The IL to the destination ports and the undesirable polarization CT versus θ_1 and θ_2 are plotted in Fig. 2. One can see in Fig. 2(a)–(c) that the $\mathrm{IL_{TE}}$, $\mathrm{CT_{TE}}$ and $\mathrm{IL_{TM}}$ reach the optimal value around $\theta_1 = 79.5^\circ$ and $\theta_2 = 85.5^\circ$ (see solid red spot in Fig. 2). Only the best $\mathrm{CT_{TM}}$ [see Fig. 2(d)] is not at the solid red spot but still close to it. As a compromise, the vertical HPW bending angle θ_1 and θ_2 are designed as 79.5° and 85.5°, respectively. Fig. 3 shows the IL and CT varying with the horizontal HPW bending angle θ_3 and θ_4. It can be found that the $\mathrm{CT_{TE}}$ [see Fig. 3(b)], $\mathrm{IL_{TM}}$ [see Fig. 3(c)], and $\mathrm{CT_{TM}}$ [see Fig. 3(d)] approach the best value around $\theta_3 = 79^\circ$ and $\theta_4 = 84^\circ$, where the solid red spot is marked, only the

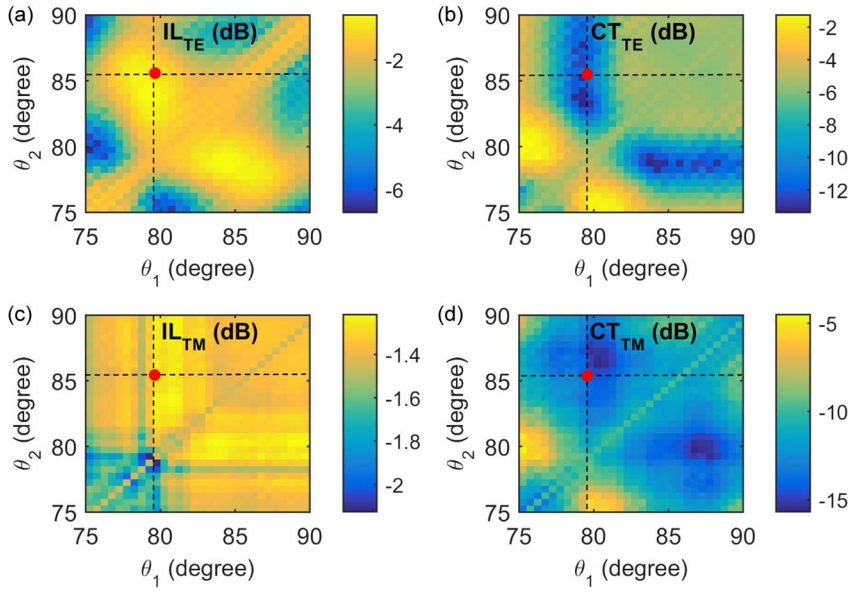

Fig. 2. IL and CT versus the vertical HPW bending angle θ_1 and θ_2. (a) IL_{TE} and (b) CT_{TE} with TE input mode. (c) IL_{TM} and (d) CT_{TM} with TM input mode.

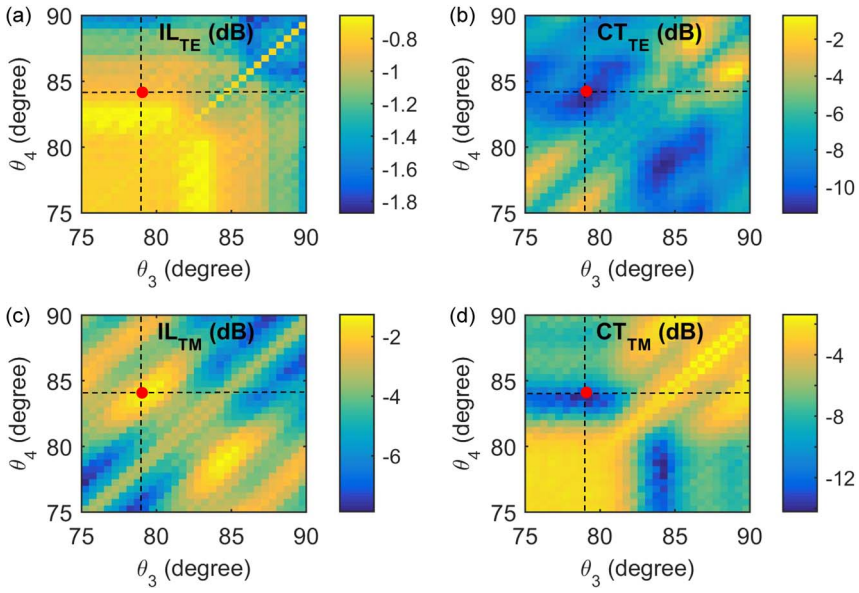

Fig. 3. IL and CT varying with the horizontal HPW bending angle θ_3 and θ_4. (a) IL_{TE} and (b) CT_{TE} with TE input mode. (c) IL_{TM} and (d) CT_{TM} with TM input mode.

lowest IL of TE mode [see Fig. 3(a)] is not right at but still close to the optimal point. Therefore, these two angles are selected as the optimized parameters for the horizontal HPW to make a trade-off. While calculating the influence of θ_3 and θ_4 on the device performance, θ_1 and θ_2 are chosen as 79.5° and 85.5°. In these simulations, the working wavelength λ is chosen as 2 μm and the other parameters are set as $W = 0.65$ μm, $W_h = 0.5$ μm, $W_v = 0.65$ μm, $H = 0.34$ μm, $H_{Ag} = 0.1$ μm, $W_{Ag} = 0.1$ μm, $W_s = 30$ nm, and $H_s = 35$ nm. The material refractive index are chosen with the consideration of material dispersion and loss [19]. In the following simulations and

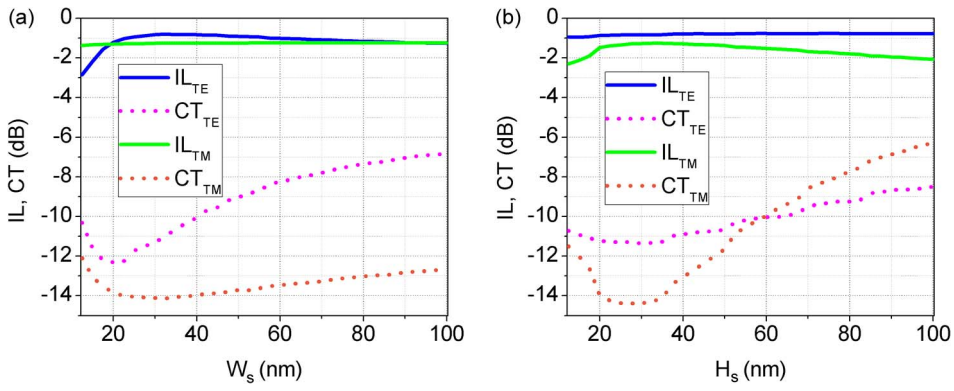

Fig. 4. IL and CT varying with (a) W_s and (b) H_s.

analysis, θ_1, θ_2, θ_3, and θ_4 are set as the optimized value of 79.5°, 85.5°, 79°, and 84°, respectively.

Since the hybrid structure used in the PBS takes both advantages of all-dielectric photonics and plasmonics for relatively low loss and compact footprint, the thickness of the lower refractive index layer (SiO_2) has a large effect on the device performance. At the wavelength around 2 μm, the absorption loss of Ag is large indicated by Drude model [11]. The effect of Ag on the HPMs should be neither too strong (inducing large IL) nor too weak (unable to excite the HPMs efficiently, in other words, the HPMs will cut-off). An appropriate HPM can be obtained by controlling the thickness of SiO_2 sandwiched in Si and Ag. Fig. 4(a) shows the dependence of the IL and CT on the SiO_2 width (W_s) of the vertical HPW. The CT_{TE} to P_3 is found to be lower than −12 dB when $W_s = 22.5$ nm, and the IL_{TE} to P_2 also approaches a relatively low value of −1 dB. For W_s less than 22.5 nm, the absorption loss of the plasmonics increases with the decreasing W_s and leads to a larger IL. On the other hand, when W_s is beyond 22.5 nm, the vertical HPM cannot be excited substantially by the incoming TE mode, and consequently, the IL increases. Meanwhile, the leakage of optical power to P_3 results in a higher CT_{TE}. A similar trend is found for IL_{TM} and CT_{TM} in Fig. 4(a). We can see that the performance deterioration rates of IL_{TM} and CT_{TM} are not as significant as those of IL_{TE} and CT_{TE} when the W_s deviates from the optimal value of 22.5 nm. It indicates that the width of the vertical slot SiO_2 has a larger influence on the vertical HPM than the horizontal HPM. The IL and CT varying with the SiO_2 thickness (H_s) of the horizontal HPW are shown in Fig. 4(b). As seen in it, the optimal IL_{TM} of −1.3 dB is obtained (with the CT_{TM} of −14.2 dB) at $H_s = 32.5$ nm. The IL_{TM} and CT_{TM} deteriorates while H_s deviate from 32.5 nm. The reason for it is the same as that for the IL_{TE} and CT_{TE} deterioration caused by W_s variation. When H_s drifts from 32.5 nm, the modest change of IL_{TE} and CT_{TE} coveys that the effect of the horizontal slot SiO_2 thickness on the horizontal HPM is stronger than that on the vertical HPM.

The influence of the width/thickness of Ag sandwiched in Si and SiO_2 on the IL and CT is simulated and analyzed. Fig. 5(a) shows the IL and CT varying with the width of Ag beside the Si waveguide at the bottom arm of the HPYB. We can see that the IL_{TE} and CT_{TE} decrease with increasing T_{Ag}. They deteriorate drastically when T_{Ag} blow 50 nm. For $T_{Ag} > 100$ nm, they are almost consistent. The CT_{TM} has an optimal value at $T_{Ag} = 50$ nm, but its increase is very limited for $T_{Ag} > 50$ nm. The IL_{TM} has little change over T_{Ag}, implying that T_{Ag} has larger influence on the vertical HPM than the horizontal HPM. Fig. 5(b) shows the IL and CT varying with the thickness of Ag above the Si waveguide at up arm of the HPYB. As seen from it, the IL_{TE} is almost unaffected by changing H_{Ag}, while IL_{TM} increases at first then decreases with increasing H_{Ag}. On the contrary to IL_{TM}, the CT_{TE} and CT_{TM} decrease at first, then increase with increasing H_{Ag}. However, the changes in the magnitude are rather modest, even for $H_{Ag} < 50$ nm. Based on the simulation results, T_{Ag} and H_{Ag} are both chosen as 100 nm to make a trade-off. In this

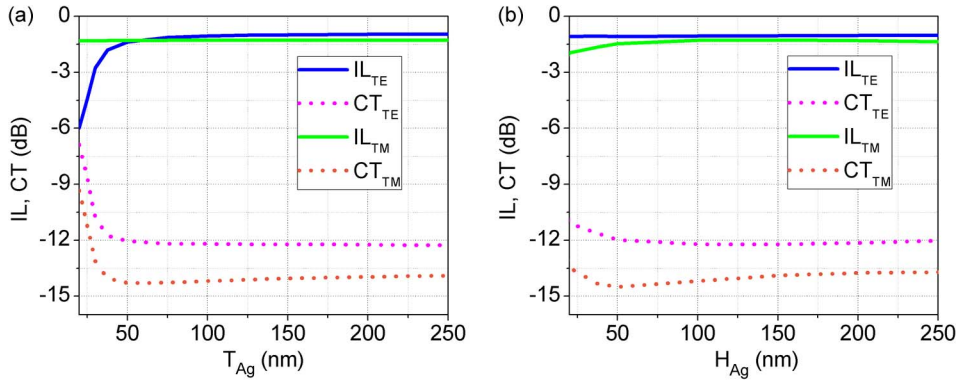

Fig. 5. IL and CT varying with (a) $_{Ag}$ and (b) H_{Ag}.

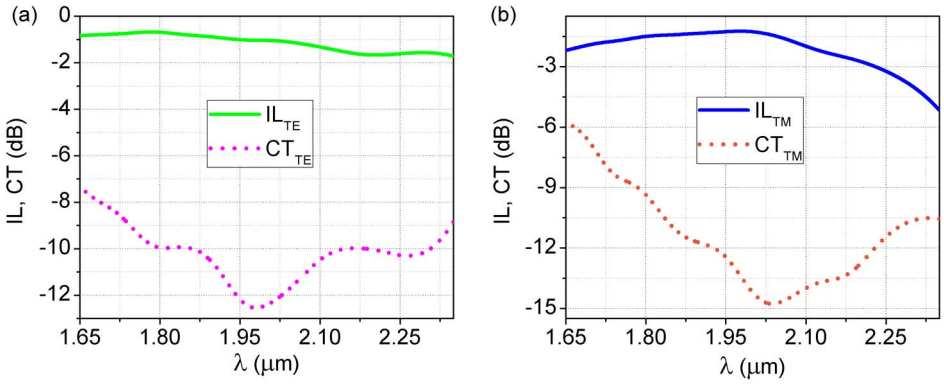

Fig. 6. Wavelength dependence of IL and CT with (a) TE input mode and (b) TM input mode.

simulation, the optimized $W_s = 22.5$ and $H_s = 32.5$ nm are used, the other dimension parameters are set as those stated previously.

The PBS is wavelength insensitive because the excitation of HPMs in the HPYB is weakly related to the input light wavelengths. Fig. 6 illustrates the input wavelength dependence of the IL and CT for the PBS. An IL of –1 (–1.3) dB, CT of –12.4 (–14.2) dB for the TE (TM) mode are obtained at the mid-infrared wavelength of 2 μm. The PBS keeps a CT < -10 dB over an ultrawide spectral range of 285 nm from 1.861 to 2.146 μm for the TE input mode. Maintaining the same CT, for the TM mode, the working bandwidth is 409 nm from 1.82 to 2.229 μm. For shorter wavelengths, i.e. $\lambda < 1.861$ μm, the electrical field confinement of the Si waveguide is becoming stronger, resulting in inefficient excitation of the HPMs by the launched lights. It indicates that the HPMs will approach cut-off and are changing into the Si channel modes, which result in smaller polarization selection. Consequently, the HPMs are unable to be split to different ports efficiently and result in the larger CT. For longer wavelengths, i.e. $\lambda > 2.146$ μm, the electrical field confinement of Si waveguide becomes weaker. As a result, the metal absorption deteriorates the device's IL and CT. Hence, for the given CT < -10 dB, the proposed PBS is able to work within an ultra-broad bandwidth of 285 nm, where the worst-case IL_{TE} and IL_{TM} are –1.53 and –2.35 dB, respectively.

In order to demonstrate the polarization splitting function with the optimized dimension parameters, the light propagation of the designed PBS for TE (E_y) and TM (E_z) modes of input are simulated and shown in Fig. 7. One can see from Fig. 7(a) that the input TE-polarization light excites the vertical HPM in the bottom arm of the HPYB. After a short distance propagation through the HPW, the vertical HPM is coupled back to the TE-polarization Si strip waveguide

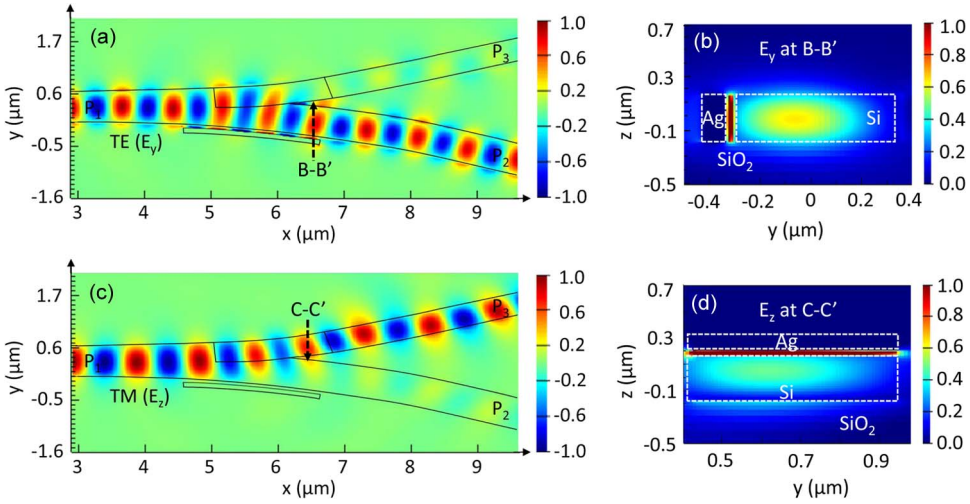

Fig. 7. (a) Light propagation and (b) electrical field at cross section B-B' with TE input mode. (c) Light propagation and (d) electrical field at cross section C-C' with TM input mode.

mode and subsequently transmits to P_2. The corresponding E_y of cross-section B-B' is shown in Fig. 7(b). It can be seen that most of the electric field is distributed in the SiO_2 slot, which forms the vertical HPM. For the TM polarization [see Fig. 7(c)], however, the input light excites the horizontal HPM [see electrical field at cross section C-C' in Fig. 7(d)] in the up arm, and then it transforms back to the TM mode after passing through the HPW and propagates to P_3. The simulation results clearly indicate that such a compact HPYB is sufficient to ensure the two HPMs are generated and split to different ports. Based on the values extracted from Fig. 7, the footprint of the PBS is estimated as $5 \times 1.8\ \mu m^2$ (x from 3 to 8 μm and y from –0.6 to 1.2 μm).

3. Fabrication Tolerance Discussion

The experimental realization of Ag strip (using the Ag strip beside Si waveguide for instance) and Si waveguides is as following: The Si waveguides will be patterned by electron beam lithography (EBL), followed by reactive-ion etching (RIE) process. To fabricate the Ag strip in the vertical HPW, "lift-off" process could be employed. A 500 nm thick of PMMA layer (950PMMA A7), which is a commonly used EBL positive resist with high resolution of sub-100 nm, will be deposited and patterned by EBL. The next step is to deposit Ag film with a thickness of 340 nm by using electron beam evaporation. After that, the sacrificial PMMA layer will be removed by PG remover or acetone, together with parts of Ag film covering it. The Ag strip is therefore formed. During the device fabrication, the actual device dimension may deviate from the designed values due to process variations and result in performance deterioration. The most probable dimension variation caused by the fabrication error is the waveguide width in the etching processes. Here, the fabrication tolerance to the waveguide width variation of the designed PBS is analyzed. We assume the width of the input waveguide (W), the bottom arm (W_v) and the up arm (W_h) of the PBS have the same deviation of ΔW induced by the fabrication error [15]. As shown in Fig. 8(a), an $IL_{TE} < -2$ dB and a $CT_{TE} < -10$ dB for the TE polarization input mode are observed with ΔW ranging from –100 to 120 nm. The IL_{TE} and CT_{TE} deteriorate as the absolute value of ΔW becomes larger. While for the TM polarization input, the device keeps the $IL < -2$ dB and $CT < -10$ dB with ΔW fluctuating from –100 to 110 nm, as seen from Fig. 8(b). The fabrication tolerance of 210 nm variation to the waveguide width is larger than that of the all-dielectric waveguide and HPW based PBSs reported in [3]–[6], [8], [9], and [15], which ensures high robustness for the fabrication of the proposed device.

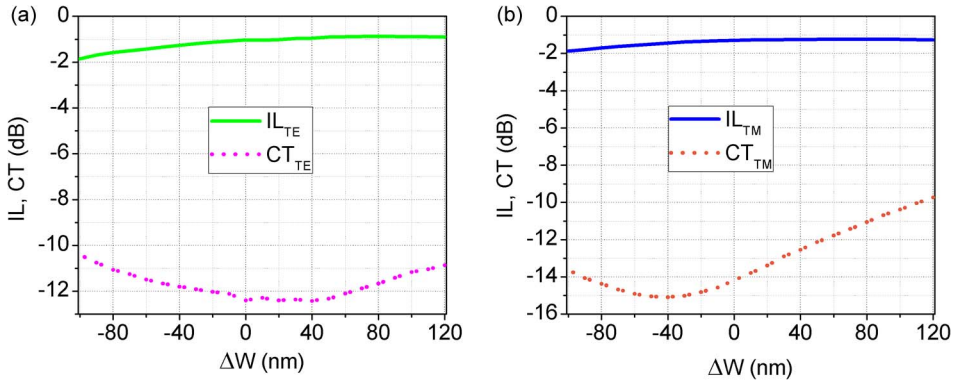

Fig. 8. Fabrication tolerance of the waveguide width variation ΔW with (a) TE input mode and (b) TM input mode.

4. Conclusion

In summary, a HPYB based PBS with the operating principle different from previous work has been proposed and numerically demonstrated. The HPYB is constructed by two bending Ag-SiO_2-Si HPWs. The influence of the starting/ending angles of Ag strip waveguide and the thickness of Ag, SiO_2 on the device performance has been analyzed by 3-D FDTD method. With the optimized dimension parameters, the device exhibits an ultra-broad bandwidth of 285 nm with 10 dB ER, while possesses a small footprint comparable to the most compact PBSs reported previously. Our numerical simulation has also shown that the fabrication tolerance of the waveguide width is greatly enhanced as compared to other HPW and all-dielectric waveguide based PBSs. These advantages enable wide potential applications of this PBS in SOI based integrated photonic circuits within the near- and mid-infrared wavelength range.

Acknowledgment

The authors would like to thank Dr. Z. Zhuang for discussing the 3-D schematic diagram drawing.

References

[1] D. Dai, L. Liu, S. Gao, D. X. Xu, and S. He, "Polarization management for silicon photonic integrated circuits," *Laser Photon. Rev.*, vol. 7, no. 3, pp. 303–328, 2013.
[2] D. Dai, Z. Wang, J. Petters, and J. E. Bowers, "Compact polarization beam splitter using an asymmetrical Mach–Zehnder interferometer based on silicon-on-insulator waveguides," *IEEE Photon. Technol. Lett.*, vol. 24, no. 8, pp. 673–675, Apr. 2012.
[3] H. Qiu, Y. Su, P. Yu, T. Hu, J. Yang, and X. Jiang, "Compact polarization splitter based on silicon grating-assisted couplers," *Opt. Lett.*, vol. 40, no. 9, pp. 1885–1887, May 2015.
[4] T. Hu *et al.*, "A polarization splitter and rotator based on a partially etched grating-assisted coupler," *IEEE Photon. Technol. Lett.*, vol. 28, no. 8, pp. 911–914, Apr. 2016.
[5] Y. Zhang *et al.*, "High-extinction-ratio silicon polarization beam splitter with tolerance to waveguide width and coupling length variations," *Opt. Exp.*, vol. 24, no. 6, pp. 6586–6593, Mar. 2016.
[6] Y. Xu and J. Xiao, "Compact and high extinction ratio polarization beam splitter using subwavelength grating couplers," *Opt. Lett.*, vol. 41, no. 4, pp. 773–776, Feb. 2016.
[7] D. W. Kim, M. H. Lee, Y. Kim, and K. H. Kim, "Planar-type polarization beam splitter based on a bridged silicon waveguide coupler," *Opt. Exp.*, vol. 23, no. 2, pp. 998–1004, Jan. 2015.
[8] X. Sun, M. Z. Alam, J. S. Aitchison, and M. Mojahedi, "Compact and broadband polarization beam splitter based on a silicon nitride augmented low-index guiding structure," *Opt. Lett.*, vol. 41, no. 1, pp. 163–166, Jan. 2016.
[9] A. Hosseini, S. Rahimi, X. Xu, D. Kwong, J. Covey, and R. T. Chen, "Ultracompact and fabrication-tolerant integrated polarization splitter," *Opt. Lett.*, vol. 36, no. 20, pp. 4047–4049, 2011.
[10] B. Shen, P. Wang, R. Polson, and R. Menon, "An integrated-nophotonics polarization beamsplitter with 2.4 $\times$ 2.4 μm^2 footprint," *Nature Photon.*, vol. 9, pp. 378–382, 2015.
[11] Q. Tan, X. Huang, W. Zhou, and K. Yang, "A plasmonic based ultracompact polarization beam splitter on silicon-on-insulator waveguides," *Sci. Rep.*, vol. 3, 2013, Art. no. 2206.

[12] S. Kim and M. Qi, "Copper nanorod array assisted silicon waveguide polarization beam splitter," *Opt. Exp.*, vol. 22, no. 8, pp. 9508–9516, Apr. 2014.
[13] R. F. Oulton, V. J. Sorger, D. A. Genov, D. F. P. Pile, and X. Zhang, "A hybrid plasmonic waveguide for subwavelength confinement and long-range propagation," *Nature Photon.*, vol. 2, pp. 496–500, 2008.
[14] D. Dai and S. He, "A silicon-based hybrid plasmonic waveguide with a metal cap for a nano-scale light confinement," *Opt. Exp.*, vol. 17, no. 19, pp. 16646–16653, Sep. 2015.
[15] X. Guan, H. Wu, Y. Shi, L. Wosinski, and D. Dai, "Ultracompact and broadband polarization beam splitter utilizing evanescent coupling between a hybrid plasmonic waveguide and a silicon nanowire," *Opt. Lett.*, vol. 38, no. 16, pp. 3005–3008, Aug. 2013.
[16] Y. Ma, G. Farrell, Y. Semenova, H. P. Chan, H. Zhang, and Q. Wu, "Low loss, high extinction ration and ultra-compact plasmonic polarization beam splitter," *IEEE Photon. Technol. Lett.*, vol. 26, no. 7, pp. 660–663, Apr. 2014.
[17] R. Soref, "Mid-infrared photonics in silicon and germanium," *Nature Photon.*, vol. 4, pp. 495–497, 2010.
[18] J. J. Coleman, A. C. Bryce, and C. Jagadish, *Advances in Semiconductor Lasers*. Amsterdam, The Netherlands: Elsevier, 2012.
[19] E. D. Palik, *Handbook of Optical Constants of Solids*. New York, NY, USA: Elsevier, 1997.